

# WO<sub>3</sub>@Fe<sub>2</sub>O<sub>3</sub> Core-Shell Heterojunction Photoanodes for Efficient Photoelectrochemical Water Splitting

Guobing Mao<sup>1</sup>, Heng Wu<sup>1,4</sup>, Tianyang Qiu<sup>2</sup>, Dingjie Bao<sup>1</sup>, Longjie Lai<sup>1</sup>, Wenguang Tu<sup>3\*</sup> and Qi Liu<sup>1\*</sup>

<sup>1</sup>School of Materials Science and Engineering, Anhui Polytechnic University, Wuhu, Anhui 241000, China

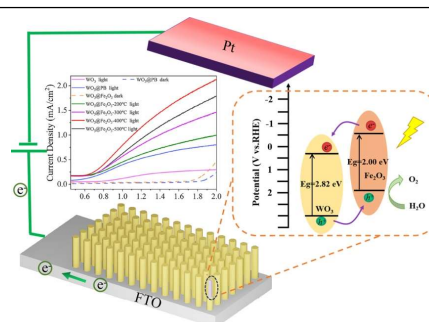
<sup>2</sup>Key Laboratory of Modern Acoustics (MOE), Institute of Acoustics, School of Physics, Eco-materials and Renewable Energy Research Center (ERERC), National Laboratory of Solid State Microstructures, Collaborative Innovation Center of Advanced Microstructures, Jiangsu Key Laboratory for Nano Technology, Nanjing University, Nanjing 210093, China

<sup>3</sup>School of Science and Engineering, The Chinese University of Hong Kong, Shenzhen, Guangdong 518172, China

<sup>4</sup>School of Mechanical Engineering, Anhui Institute of Information Technology, Wuhu, Anhui 241100, China

**ABSTRACT** Photoelectrochemical (PEC) hydrogen production from water splitting is a green technology to convert solar energy into renewable hydrogen fuel. The construction of host/guest architecture in semiconductor photoanodes has been proven to be an effective strategy to improve solar-to-fuel conversion efficiency. In this study, WO<sub>3</sub>@Fe<sub>2</sub>O<sub>3</sub> core-shell nanoarray heterojunction photoanodes are synthesized from the *in-situ* decomposition of WO<sub>3</sub>@Prussian blue (WO<sub>3</sub>@PB) and then used as host/guest photoanodes for photoelectrochemical water splitting, during which Fe<sub>2</sub>O<sub>3</sub> serves as guest material to absorb visible solar light and WO<sub>3</sub> can act as host scaffolds to collect electrons at the contact. The prepared WO<sub>3</sub>@Fe<sub>2</sub>O<sub>3</sub> shows the enhanced photocurrent density of 1.26 mA cm<sup>-2</sup> (under visible light) at 1.23 V. vs RHE and a superior IPEC of 24.4% at 350 nm, which is higher than that of WO<sub>3</sub>@PB and pure WO<sub>3</sub> (0.43 mA/cm<sup>2</sup> and 16.3%, 0.18 mA/cm<sup>2</sup> and 11.5%) respectively, owing to the efficient light-harvesting from Fe<sub>2</sub>O<sub>3</sub> and the enhanced electron-hole pairs separation from the formation of type-II heterojunctions, and the direct and ordered charge transport channels from the one-dimensional (1D) WO<sub>3</sub> nanoarray nanostructures. Therefore, this work provides an alternative insight into the construction of sustainable and cost-effective photoanodes to enhance the efficiency of the solar-driven water splitting.

**Keywords:** host/guest photoelectrodes, WO<sub>3</sub>, α-Fe<sub>2</sub>O<sub>3</sub>, core-shell nanostructures, one-dimensional nanoarray



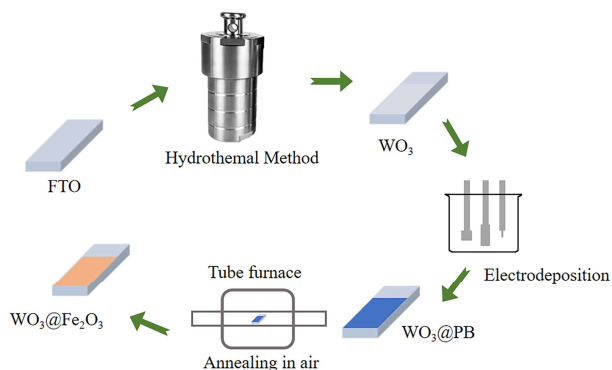
## INTRODUCTION

Converting solar energy into renewable chemical fuels has been proven as one of the promising approaches to tackle the critical energy challenges and the environmental problems.<sup>[1,2]</sup> Photoelectrochemical (PEC) splitting water into hydrogen fuel conducted by semiconductor-based photoelectrodes can realize the storage of solar energy in the form of chemical energy.<sup>[3]</sup> Since Fujishima and Honda firstly conducted the pioneering PEC water splitting via TiO<sub>2</sub> films as the photoanodes, significant efforts have been made to explore appropriate semiconductor-based photoanodes to conduct efficient PEC water splitting from the factors such as the solar energy harvesting, the diffusion length of the charge carriers, and the photoanode stability. However, using single semiconductors such as TiO<sub>2</sub>, WO<sub>3</sub>, ZnO and α-Fe<sub>2</sub>O<sub>3</sub> as photoanodes is difficult to meet the critical factors of PEC water splitting simultaneously.<sup>[4-7]</sup> For example, compared with the semiconductors with smaller band gap, the material with larger band gap possesses resistance photocorrosion, but the weakened light absorption capacity limits the improvement of PEC performance.<sup>[8-10]</sup>

Among the semiconductor materials for PEC water splitting, WO<sub>3</sub> is the widely researched n-type semiconductor due to its excellent optical properties, stability, and suitable band structure (of 2.5-2.8 eV).<sup>[11]</sup> WO<sub>3</sub> not only possesses high electron hole mobility (12 cm<sup>2</sup> V<sup>-1</sup> s<sup>-1</sup>) but also has deep carry diffusion length (~150 nm). However, the insufficient visible light adsorption restricts the im-

proved efficiency of PEC water splitting.<sup>[12-14]</sup> Inspired by the synergistic effects of a tree trunk for mass transport and leaves for light absorption in natural photosynthesis, host/guest multicomponent architectures have been explored for efficient PEC water splitting, during which a highly dispersed light absorber acting as the guest material is deposited onto nanostructured host scaffolds.<sup>[15-17]</sup> Recently, combining WO<sub>3</sub> with other semiconductors to construct host/guest heterojunction structure, such as g-C<sub>3</sub>N<sub>4</sub>/WO<sub>3</sub>,<sup>[17,18]</sup> TiO<sub>2</sub>/WO<sub>3</sub>,<sup>[19-22]</sup> and WO<sub>3</sub>/α-Fe<sub>2</sub>O<sub>3</sub>,<sup>[23-25]</sup> can effectively improve the visible light adsorption and the transfer of charge carriers, thus achieving considerable PEC performance. Furthermore, one-dimensional (1D) nanostructure arrays with a reduced quantity of defects and fewer grain boundaries could provide direct and ordered channels for charge transport.<sup>[26-29]</sup>

Here, we report a novel and facile method to prepare WO<sub>3</sub>@Fe<sub>2</sub>O<sub>3</sub> core-shell nanoarray heterojunction photoanodes via *in situ* transformation from WO<sub>3</sub>@Prussian blue (WO<sub>3</sub>@PB), during which WO<sub>3</sub>@PB on fluorine-doped tin oxide (FTO) was prepared by the hydrothermal growth of WO<sub>3</sub> nanorod arrays and subsequent electrodeposition of PB layer on WO<sub>3</sub> nanorod arrays. The optimized WO<sub>3</sub>@Fe<sub>2</sub>O<sub>3</sub> prepared at 400 °C achieves the enhanced PEC performance with the photocurrent density of 1.26 mA cm<sup>-2</sup> at 1.23 V. vs RHE and a superior IPEC of 24.4% at 350 nm, which is higher than that of WO<sub>3</sub>@PB and pure WO<sub>3</sub> (0.43 mA/cm<sup>2</sup> and 16.3%, 0.18 mA/cm<sup>2</sup> and 11.5%), respectively. It indicates that the formation of host/guest architecture in WO<sub>3</sub>@Fe<sub>2</sub>O<sub>3</sub> core-shell



**Scheme 1.** Schematic illustration of the synthesis process of  $\text{WO}_3@Fe_2O_3$ .

nanoarray heterojunction photoanode induces the efficient light-harvesting from the  $Fe_2O_3$  with the narrow bandgap as guest material, the enhanced electron-hole pairs separation from the formation of type-II heterojunctions, and the direct and ordered charge transport channels from the 1D host  $WO_3$  nanoarray nanostructures. This work provides an alternative insight into the construction of sustainable and cost-effective photo-anodes to enhance the efficiency of the solar-driven water splitting.

## RESULTS AND DISCUSSION

The synthesized processes of  $\text{WO}_3@Fe_2O_3$  core-shell nanorod array heterojunction photoanodes are shown in Scheme 1. Firstly,  $WO_3$  seed layer was got by spin-coating the tungstic acid solution on FTO glass and then annealing in the muffle furnace. Then,  $WO_3$  nanorod arrays were vertically aligned on FTO surface by the hydrothermal method.<sup>[30]</sup> Subsequently, the PB layer was deposited on the surface of  $WO_3$  nanorod arrays via the simple electrochemical deposition method<sup>[31]</sup> to form  $\text{WO}_3@PB$  nanorod arrays. Finally, PB on  $WO_3$  surface would in situ transform into  $Fe_2O_3$  by the annealing treatment to obtain  $\text{WO}_3@Fe_2O_3$  core-

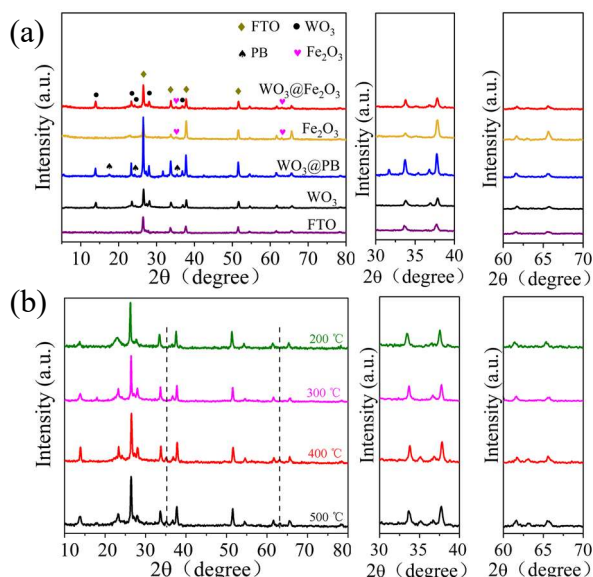


**Figure 1.** XRD and partial enlarged XRD patterns of (a) FTO,  $WO_3$ ,  $WO_3@PB$ ,  $Fe_2O_3$ , and  $WO_3@Fe_2O_3$ . (b)  $WO_3@Fe_2O_3$  prepared at different heat treatment temperatures.

shell nanorod array heterojunction photoanodes.

The phases of as prepared samples are determined by the powder X-ray diffraction (XRD) patterns (Figure 1a). The diffraction peaks of  $WO_3$  film are indexed to hexagonal-phase  $WO_3$  (JCPDS 85-2460). Compared to pure  $WO_3$  film, all characteristic peaks of  $WO_3@PB$  film are attributable to  $WO_3$  (JCPDS 85-2460) and  $Fe_4[Fe(CN)_6]_3$  (JCPDS 01-0239),<sup>[32-34]</sup> indicating the successful deposition of PB nanoparticles on the  $WO_3$  nanorod arrays. For  $Fe_2O_3$  thin film directly prepared from the annealing treatment of PB film, there are two characteristic peaks at  $35^\circ$  and  $63^\circ$ , which can be well assigned to the (201) and (220) planes of hexagonal  $Fe_2O_3$  (JCPDS 40-1139). The characteristic peaks of hexagonal  $Fe_2O_3$  also appear in the  $WO_3@Fe_2O_3$  sample and no other redundant peaks appear, indicating that the PB completely transformed into  $Fe_2O_3$  on the surface of  $WO_3$  nanorod arrays. In order to explore the effect of heat temperature on the sample treatment,  $WO_3@PB$  samples were annealed at 200, 300, 400 and 500  $^\circ C$ . The calcination temperature has a significant effect on the phase structure of the final products. No corresponding characteristic peaks of  $Fe_2O_3$  were observed (Figure 1b), because the PB transformed into amorphous  $Fe_2O_3$  after the heat treatment at 200 and 300  $^\circ C$ .<sup>[35-37]</sup> Hu et al.<sup>[36]</sup> calcined PB with a particle size about 100-150 nm at 250  $^\circ C$ , and amorphous  $Fe_2O_3$  was obtained. As the calcination temperature increases, the phase of the final products changes from amorphous to crystal. When rising to 400 and 500  $^\circ C$ , the corresponding characteristic peaks located at  $35^\circ$  and  $63^\circ$  were observed, indicating the crystalline  $Fe_2O_3$  formed on the surface of  $WO_3$  nanorod arrays.

As shown in Figure 2a, the scanning electron microscopy (SEM) image illustrates the uniform polygonal morphology of  $WO_3$  nanorod arrays with the diameter of approximately 100 nm. The surface of  $WO_3$  nanorod arrays becomes rough (Figure 2b) after the in situ deposition of PB, indicating the successful growth of PB nanoparticles on the  $WO_3$  nanorod arrays. The morphology of  $WO_3$  nanorod arrays is well preserved after the heat treatment for preparing  $WO_3@Fe_2O_3$  nanorod arrays (Figure 2c, d). The surface of  $WO_3@Fe_2O_3$  nanorod arrays becomes rougher with abundant pores, which greatly improves the specific surface area of  $WO_3@Fe_2O_3$  nanorod arrays, resulting in more exposed catalytic

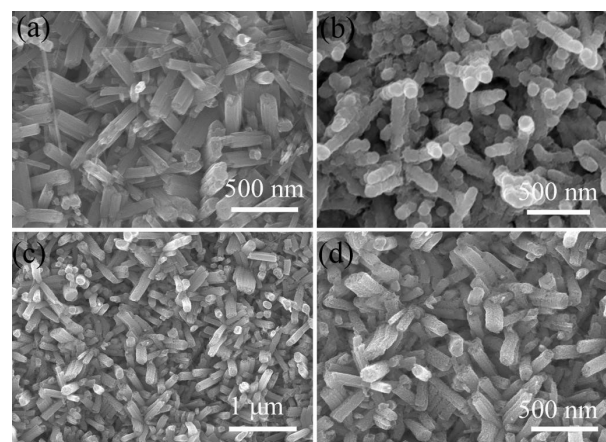


**Figure 2.** SEM images of (a)  $WO_3$ , (b)  $WO_3@PB$ , and (c, d)  $WO_3@Fe_2O_3$  prepared at 400  $^\circ C$ .

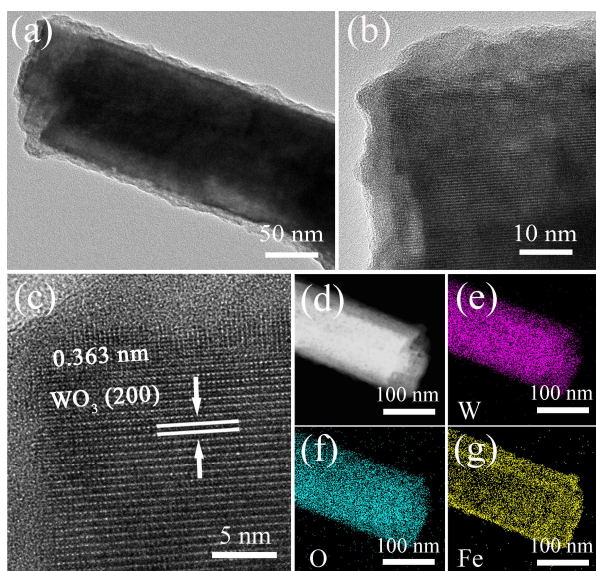


**Figure 3.** TEM images of (a,b)  $\text{WO}_3@Fe_2O_3$ , (c) HRTEM image of  $\text{WO}_3@Fe_2O_3$ , (d-g) Elemental mapping images of  $\text{WO}_3@Fe_2O_3$ .

sites. Moreover, the porous structure could lead to the reflection and absorption of light, probably improving the photon absorption efficiency.

The high-resolution TEM (HRTEM) image (Figure 3a) showed one single  $\text{WO}_3$  nanorod with a diameter of about 120 nm. Moreover, the ultra-small  $\text{Fe}_2O_3$  nanoparticles are uniformly distributed on the surface of  $\text{WO}_3$  nanorod to form a porous shell with a thickness of about 10 nm (Figure 3a, b). As shown in Figure 3c, the lattice fringe with an interplanar spacing of 0.365 nm is corresponding to (200) crystallographic plane of hexagonal  $\text{WO}_3$ . TEM-energy-dispersive X-ray spectrometry (EDS) elemental mappings (Figure 3d-g) furtherly confirmed the uniform distribution of  $\text{Fe}_2O_3$  nanoparticles on the surface of  $\text{WO}_3$  nanorod.

X-ray photoelectron spectroscopy (XPS) analysis was employed to further investigate the valence state of all atoms (Figure 4). The survey spectrum suggests the presence of W, O and Fe elements

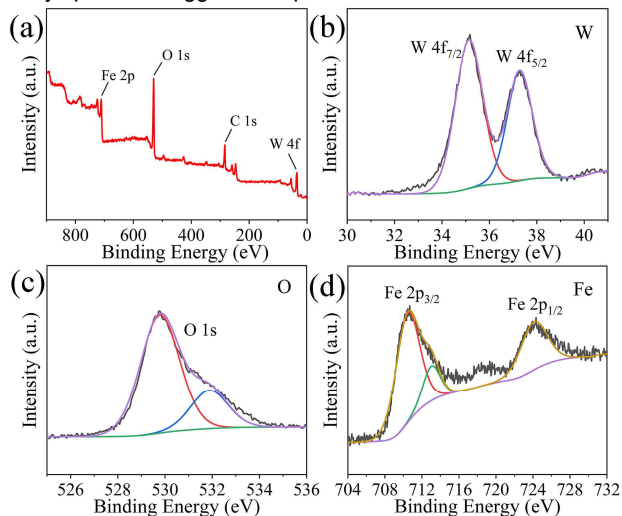


**Figure 4.** XPS analysis of  $\text{WO}_3@Fe_2O_3$ : (a) survey spectra, (b) W 4f, (c) O 1s, (d) Fe 2p.

in  $\text{WO}_3@Fe_2O_3$  heterojunction (Figure 4a). The high-resolution XPS spectra of W 4f (Figure 4b) show two characteristic peaks of W  $4f_{7/2}$  at 35.8 and W  $4f_{5/2}$  at 37.4 eV, indicating the oxidation state of  $W^{6+}$ .<sup>[38]</sup> The O 1s spectrum of the sample can be subdivided into one peak at 531.9 eV attributed to the adsorption of water and oxygen from hydroxide on the surface<sup>[39,40]</sup> and the other strong peak at 529.8 eV belonging to the lattice oxygen of metal oxide (Figure 4c). The Fe 2p spectra at higher resolution (Figure 4d) exhibit two binding energy peaks at 724.4 eV (Fe  $2p_{1/2}$ ) and 710.8 eV (Fe  $2p_{3/2}$ ) with a characteristic satellite peak at 719.1 eV, which is the typical characteristic of  $Fe^{3+}$ . Therefore, the successful fabrication of the  $\text{WO}_3@Fe_2O_3$  composite can be confirmed.

The PEC performances of the fabricated electrodes were measured in a three-electrode electrochemical cell with 0.1 M  $\text{Na}_2\text{SO}_4$  as electrolyte under irradiation using a 300 W Xe arc lamp with a UV cutoff filter ( $\lambda > 420$  nm) (Figure 5). The photoelectric response of the prepared electrodes was evaluated by linear sweep voltammograms (LSV) (Figure 5a). The photocurrent of  $\text{WO}_3@Fe_2O_3$  increases with the increase of treatment temperature from 200 to 400 °C and then decreases from 400 to 500 °C. The photocurrent density of  $\text{WO}_3@Fe_2O_3$ -400 photoanode is continuously strong in the linearly swept from 0.6 to 2.0 V (RHE) in comparison with the others, indicating that 400 °C is the optimal temperature for sample treatment. The transient photo-current curves of as-synthesized photoanodes at 1.23 V (vs. RHE) under light irradiation were presented in Figure 5b. For all the photoanodes, the photocurrents appeared under light irradiation and then disappeared once the light was turned off, implying rapid photoresponsive properties of the obtained photoanodes. The photocurrent density of  $\text{WO}_3@Fe_2O_3$  treated at 200, 300, 400 and 500 °C are 0.68, 0.80, 1.26 and 0.98  $\text{mA}/\text{cm}^2$ , respectively. The highest photocurrent density up to 1.26  $\text{mA}/\text{cm}^2$  was obtained over  $\text{WO}_3@Fe_2O_3$ -400 photoanode, which is about 3.0 times that of  $\text{WO}_3@PB$  (0.43  $\text{mA}/\text{cm}^2$ ) and 7.0 times that of pure  $\text{WO}_3$  (0.18  $\text{mA}/\text{cm}^2$ ). Bare  $\text{Fe}_2O_3$  shows weak photocurrent density due to fast recombination of photogenerated carriers (Figure S1). When light reaches on the  $\text{Fe}_2O_3$  photoanode, the increase in photocurrent is accompanied by a nearly instant rapid decay. Ultrafast charge recombina-

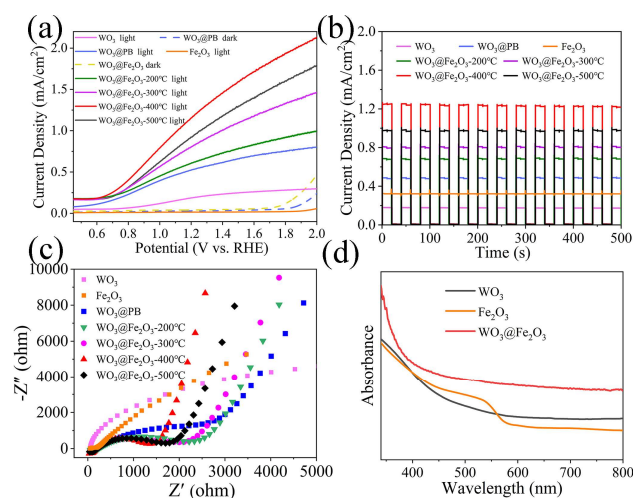


**Figure 5.** (a) LSV (scan rate: 5  $\text{mV}/\text{s}$ ), (b) photocurrent ( $I-t$ ), (c) EIS results, (d) UV-vis absorption spectra for prepared samples.

tion in  $\text{Fe}_2\text{O}_3$  can be effectively overcome by compounding with other semiconductors or doping different elements.<sup>[41-43]</sup>

The electrochemical impedance spectroscopy (EIS) measurements were employed to further investigate the charge transport kinetics of these photoanodes, as shown in Figure 5c and Figure S2. The smaller semicircle radius represents the smaller charge transfer impedance and the higher separation efficiency of the photogenerated electrons-hole pairs.<sup>[44]</sup> The semi-circle diameters of all prepared  $\text{WO}_3@Fe_2O_3$  are much smaller than that of  $\text{WO}_3@PB$  and  $\text{WO}_3$ , indicating better interface charge transfer between  $\text{WO}_3$  and  $\text{Fe}_2O_3$ .  $\text{WO}_3@Fe_2O_3-400$  shows the smallest semi-circle compared with other heat treatment temperatures, which indicates that this sample has the fastest interfacial charge transfer rate and the best separation of photogenerated electrons-hole pairs in  $\text{WO}_3@Fe_2O_3-400$ . The fitted EIS results of photoanodes are summarized in Table S1, which basically reveals the analogous variation trends in LSV and I-t results.

For photoelectrocatalysis, efficient photon utilization and matched band structure for catalytic materials are of vital importance. Thus, we utilized UV-visible (UV-vis) diffuse reflectance spectra to monitor the light adsorption capacity of pristine  $\text{WO}_3$  and  $\text{WO}_3@Fe_2O_3$  (Figure 5d). The bandgap valences of all samples are estimated by UV-vis adsorption spectra through a related curve of  $(\alpha h\nu)^{1/2}$  versus the mode of photon energy, and the bandgaps of  $\text{WO}_3$  and  $\text{Fe}_2O_3$  were calculated to be 2.82 and 2.00 eV, respectively. After  $\text{Fe}_2O_3$  was grown on the surface of  $\text{WO}_3$  nanorods to form a heterostructure, the mode of interband transition of electrons changed, resulting in the reduction of the band gap width and the enhancement of light adsorption capacity. Furthermore, the porous structure of  $\text{Fe}_2O_3$  provides a higher photon receiving area and reduces the non-utilization of optical wave caused by reflection on the material surface. To be specific, when the light shines on the surface of the nanorods, photon will enter the hole and be reflected many times in the hole until absorbed.

The incident photon-to-current conversion efficiency (IPCE) measurement was conducted to investigate the influence of light absorption. The IPCE of  $\text{WO}_3@Fe_2O_3$  increases with increasing

the treatment temperature from 200 to 400 °C and then decreasing it from 400 to 500 °C (Figure 6a), showing a similar trend with the photocurrent of  $\text{WO}_3@Fe_2O_3$ .  $\text{WO}_3@Fe_2O_3-400$  shows the highest IPCE value, which is up to 24.4% at 350 nm. The IPCE results reveal that the deposition of  $\text{Fe}_2O_3$  on the surface of  $\text{WO}_3$  enhances the light absorption capacity. Therefore, the IPCE value of  $\text{WO}_3@Fe_2O_3$  is significantly improved compared with that of  $\text{WO}_3@PB$ . These results show that host/guest approach can effectively enhance the photoelectrochemical performance of  $\text{WO}_3$  film. Gratzel et al constructed  $\text{WO}_3@Fe_2O_3$  host/guest photoanodes which show a ca. 20% increase in photocurrent as compared to  $\text{Fe}_2O_3$ .<sup>[45]</sup>  $\text{WO}_3/\text{Ti-Fe}_2O_3$  photoanode was designed with improved PEC water splitting performance owing to charge transfer enhancement of  $\text{WO}_3/\text{Fe}_2O_3$  interface.<sup>[46]</sup> This host/guest  $\text{WO}_3@Fe_2O_3$  derived from PB not only facilitates the charge separation but also boosts the light absorption.

In order to prove the charge transfer between  $\text{WO}_3$  and  $\text{Fe}_2O_3$ , the photoluminescence (PL) spectra of  $\text{WO}_3@Fe_2O_3$  have been investigated (Figure 6b). The PL intensity of  $\text{WO}_3@Fe_2O_3$  is much lower than that of  $\text{Fe}_2O_3$  and  $\text{WO}_3$  films, confirming the efficient separation of the photogenerated electrons-hole pairs. Mott-Schottky plots of pristine  $\text{WO}_3$  and  $\text{Fe}_2O_3$  films were employed to investigate the band alignment information (Figure 6c). Both Mott-Schottky plots of pristine  $\text{WO}_3$  and  $\text{Fe}_2O_3$  exhibit positive slopes, indicating the n-type semiconductor feature of  $\text{WO}_3$  and  $\text{Fe}_2O_3$ . The results display that the flat band potentials of  $\text{WO}_3$  and  $\text{Fe}_2O_3$  are 0.51 and -0.11 V, respectively. Combined with the aforementioned results of optical bandgap estimation, the conduction band (CB) and valence band (VB) positions of  $\text{WO}_3$  are calculated to be 0.42 and 3.24 eV, and the CB and VB positions of  $\text{Fe}_2O_3$  are located at -0.21 and 1.79 eV. Therefore, a possible schematic illustration for energy-level alignment of  $\text{WO}_3@Fe_2O_3$  is suggested in Figure 6d. It can be seen that  $\text{WO}_3$  and  $\text{Fe}_2O_3$  show a well staggered band alignment with the type II heterojunction. Due to the higher CB of  $\text{Fe}_2O_3$  than  $\text{WO}_3$ , the photogenerated electrons of  $\text{Fe}_2O_3$  can be immediately delivered to the CB of  $\text{WO}_3$  via the direct and ordered charge transport channels from the one-dimensional (1D)  $\text{WO}_3$  nanoarray nanostructures, while photogenerated holes of  $\text{WO}_3$  can transfer to the VB of  $\text{Fe}_2O_3$ , which hinders the fast recombination of electron-hole pairs and thus improves PEC activity.

## CONCLUSION

In summary,  $\text{WO}_3@Fe_2O_3$  core-shell nanoarray heterojunction photoanodes were prepared by *in-situ* decomposition of  $\text{WO}_3@PB$  precursor at different temperature. The optimized  $\text{WO}_3@Fe_2O_3$  prepared at 400 °C showed efficient PEC performance with the photocurrent density of 1.26 mA/cm<sup>2</sup> at 1.23 V vs. RHE, which is about 3.0 times that of  $\text{WO}_3@PB$  (0.43 mA/cm<sup>2</sup>) and 7.0 times that of pure  $\text{WO}_3$ . The efficient PEC performance of  $\text{WO}_3@Fe_2O_3$  is attributed to the construction of type-II core-shell heterojunctions, which enhances the visible light absorption and facilitates the separation of photo-generated electron-hole pairs. This work provides an alternative insight into the construction of sustainable and cost-effective photoanodes to enhance the efficiency of the solar-driven water splitting.

## EXPERIMENTAL

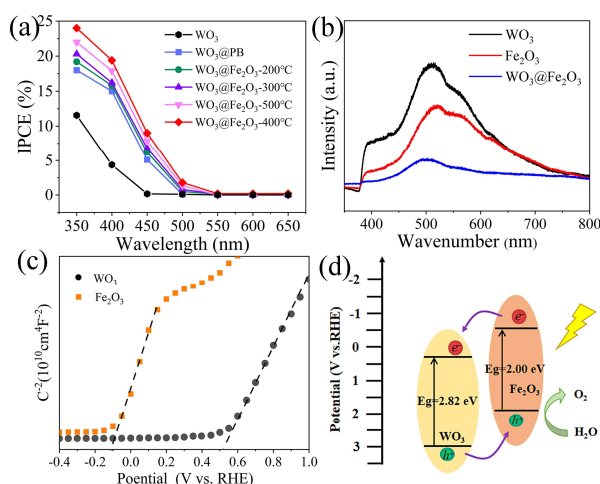


**Figure 6.** (a) IPCE plots, (b) PL of prepared samples, (c) Mott-Schottky curves of  $\text{WO}_3$  and  $\text{Fe}_2O_3$ , (d) Schematic of the charge transfer and separation in the  $\text{WO}_3@Fe_2O_3$  and the PEC working mechanism for water splitting.

**Materials.** All reagents were obtained from commercial sources and used as received without further purification.

**Synthesis of WO<sub>3</sub> and WO<sub>3</sub>@Fe<sub>2</sub>O<sub>3</sub> Films.** The WO<sub>3</sub> nanorod arrays were synthesized with the hydrothermal method modified from previously reported method.<sup>[30]</sup> The electrochemical deposition of PB layer on WO<sub>3</sub> nanorod arrays was conducted in the three-electrode system at room temperature, during which the FTO with WO<sub>3</sub> film, the platinum plate, and the Ag/AgCl were used as the working electrode, counter electrode, and reference electrode, respectively. The electrolytes were composed of 1 mM K<sub>3</sub>Fe(CN)<sub>6</sub>, 1 mM FeCl<sub>3</sub>·6H<sub>2</sub>O, and 5.0 mM KCl. The PB layers were deposited on the surface of WO<sub>3</sub> by applying a constant potential at 0.3 V for 100 s. The obtained samples were washed with deionized water and then dried at 100 °C for 1 h. Then, WO<sub>3</sub>@PB nanorod arrays were heated at the different temperature of 200, 300, 400, and 500 °C, which were defined as WO<sub>3</sub>@Fe<sub>2</sub>O<sub>3</sub>-200, WO<sub>3</sub>@Fe<sub>2</sub>O<sub>3</sub>-300, WO<sub>3</sub>@Fe<sub>2</sub>O<sub>3</sub>-400 and WO<sub>3</sub>@Fe<sub>2</sub>O<sub>3</sub>-500, respectively. The heating and cooling rates were 4 and 5 °C min<sup>-1</sup>. As a comparison, Fe<sub>2</sub>O<sub>3</sub> thin film was prepared by annealing the PB film directly.

**Characterization.** The phase structures of the prepared samples were studied with an X-ray diffractometer with Cu K $\alpha$  radiation of  $\lambda = 1.5406 \text{ \AA}$ . The Field-emission scanning electron microscopy (FESEM) was tested by S-4800 (Japan) instrument. The TEM data, elemental mapping, and energy dispersive X-ray spectroscopy (EDS) values were measured using JEOL JEM-2100 F (USA). The X-ray photoelectron spectroscopy (XPS) measurements were obtained using Thermo Fisher Scientific K-Alpha (USA), and the binding energy was calibrated with C 1s at 284.8 eV. The UV visible light adsorption spectra were using a Shimadzu UV-3600 with an 0.1 nm interval in the range of 185-800 nm, and the spectra were transformed from reflection into absorbance by the Kubelka-Munk Method. The photoluminescence spectra analysis was performed using a Horiba Fluorolog 3-22 fluorometer with an excitation wavelength of 520 nm and an emission spectrum scanning range of 550-850 nm.

**Electrochemical Measurements.** The electrochemical measurements were recorded at room temperature (25 °C) in cell quartz with a three-electrode system configurations, during which thin-film FTO, Ag/AgCl, Pt mesh, and 0.1 M Na<sub>2</sub>SO<sub>4</sub> solution were used as the working electrode, reference electrode, counter electrode, and electrolyte, respectively. The 300 W Xe lamp was used as light source by using a UV cutoff filter ( $\lambda > 420 \text{ nm}$ ) to get visible light. The Nyquist plots were measured in the frequency range between 0.01 and 10<sup>5</sup> Hz at 1.23 V vs. RHE under dark conditions with an AC voltage perturbation of 10 mV. The Mott-Schottky measurements were conducted in dark conditions at 2000 Hz.

## ACKNOWLEDGEMENTS

The work is supported by the Natural Science Foundation of Anhui Province (No. 2008085ME132), Talent Project of Anhui Province (Z175050020001), the Key Project of Anhui Provincial Department of Education (No. KJ2019A0157), the Program from Guangdong Introducing Innovative and Entrepreneurial Teams (Nos. 2019ZT08L101 and RCTDPT-2020-001), the Shenzhen Natural Science Foundation (No. GXWD20201231105722002-

20200824163747001), and Shenzhen Key Laboratory of Ecomaterials and Renewable Energy (No. ZDSYS20200922160400001).

## AUTHOR INFORMATION

Corresponding authors. Emails: modieer\_67@ahpu.edu.cn and tuwenguang@cuhk.edu.cn

## COMPETING INTERESTS

The authors declare no competing interests.

## ADDITIONAL INFORMATION

Supplementary information is available for this paper at <http://manu30.magtech.com.cn/jghx/EN/10.14102/j.cnki.0254-5861.2022-0086>

For submission: <https://mc03.manuscriptcentral.com/cjsc>

## REFERENCES

- (1) Fu, J.; Fan, Z.; Nakabayashi, M.; Ju, H.; Pastukhova, N.; Xiao, Y.; Feng, C.; Shibata, N.; Domen, K.; Li, Y. Interface engineering of Ta<sub>3</sub>N<sub>5</sub> thin film photoanode for highly efficient photoelectrochemical water splitting. *Nat. Commun.* **2022**, *13*, 729-735.
- (2) Seabold, J.; Choi, K. Effect of a cobalt-based oxygen evolution catalyst on the stability and the selectivity of photo-oxidation reactions of a WO<sub>3</sub> photoanode. *Chem. Mater.* **2011**, *23*, 1105-1112.
- (3) Liu, Y.; Yu, F.; Wang, F.; Bai, S.; He, G. Construction of Z-scheme In<sub>2</sub>S<sub>3</sub>-TiO<sub>2</sub> for CO<sub>2</sub> reduction under concentrated natural sunlight. *Chin. J. Struct. Chem.* **2022**, *41*, 2201034-2201039.
- (4) Li, C.; Li, T.; Jing, M.; Yuan, W.; Li, C. M. Remarkably promoted photoelectrochemical water oxidation on TiO<sub>2</sub> nanowire arrays via polymer-mediated self-assembly of CoO<sub>x</sub> nanoparticles. *Sol. Energ. Mat. Sol. C* **2020**, *207*, 110349.
- (5) Zou, J.; Liao, G.; Jiang, J.; Xiong, Z.; Bai, S. In-situ construction of sulfur-doped g-C<sub>3</sub>N<sub>4</sub> defective g-C<sub>3</sub>N<sub>4</sub> isotype step-scheme heterojunction for boosting photocatalytic H<sub>2</sub> evolution. *Chin. J. Struct. Chem.* **2022**, *41*, 2201025-2201033.
- (6) Yuan, W.; Yuan, J.; Xie, J.; Li, C. M. Polymer-mediated self-assembly of TiO<sub>2</sub>@Cu<sub>2</sub>O core-shell nanowire array for highly efficient photoelectrochemical water oxidation. *ACS Appl. Mater. Inter* **2016**, *8*, 6082-6092.
- (7) Zhu, P.; Wang, Y.; Sun, X.; Zhang, J.; Wacławik, E. R.; Zheng, Z. Photocatalytic-controlled olefin isomerization over WO<sub>3-x</sub> using low-energy photons up to 625 nm. *Chin. J. Catal.* **2021**, *42*, 1641-1647.
- (8) Ran, L.; Qiu, S.; Zhai, P.; Li, Z.; Gao, J.; Zhang, X.; Zhang, B.; Wang, C.; Sun, L.; Hou, J. Conformal macroporous inverse opal oxynitride-based photoanode for robust photoelectrochemical water splitting. *J. Am. Chem. Soc.* **2021**, *143*, 7402-7413.
- (9) He, J. S.; Liu, P. Y.; Ran, R.; Wang, W.; Zhou, W.; Shao, Z. P. Single-atom catalysts for high-efficiency photocatalytic and photoelectro-chemical water splitting: distinctive roles, unique fabrication methods and specific design strategies. *J. Mater. Chem. A* **2022**, *10*, 6835-6871.
- (10) Gaikwad, M. A.; Suryawanshi, U. P.; Ghorpade, U. V.; Jang, J. S.; Suryawanshi, M. P.; Kim, J. H. Emerging surface, bulk, and interface engineering strategies on BiVO<sub>4</sub> for photoelectrochemical water splitting. *Small* **2022**, *18*, 2105084.
- (11) Li, C.; Chen, Z.; Yuan, W.; Xu, Q. H.; Li, C. M. In situ growth of  $\alpha$ -Fe<sub>2</sub>O<sub>3</sub>@Co<sub>3</sub>O<sub>4</sub> core-shell wormlike nanoarrays for a highly efficient photoelectrochemical water oxidation reaction. *Nanoscale* **2019**, *11*, 1111-1122.

- (12) Pinto, F.; Wilson, A.; Moss, B.; Kafizas, A. Systematic exploration of WO<sub>3</sub>/TiO<sub>2</sub> heterojunction phase space for applications in photoelectrochemical water splitting. *J. Phys. Chem. C* **2022**, 126, 871-884.
- (13) Wang, Y.; Wang, Y.; Zhao, J.; Chen, M.; Huang, X.; Xu, Y. Efficient production of H<sub>2</sub>O<sub>2</sub> on Au/WO<sub>3</sub> under visible light and the influencing factors. *Appl. Catal. B* **2021**, 284, 119691-119702.
- (14) Liu, X.; Wanga, F.; Wanga, Q. Nanostructure-based WO<sub>3</sub> photoanodes for photoelectrochemical water splitting. *Phys. Chem. Chem. Phys.* **2012**, 14, 7894-7911.
- (15) Wang, Z.; Zhu, H.; Tu, W.; Zhu, X.; Yao, Y.; Zhou, Y.; Zou, Z. Host/guest nanostructured photoanodes integrated with targeted enhancement strategies for photoelectrochemical water splitting. *Adv. Sci.* **2022**, 9, 103744.
- (16) Francisco, F.; Dias, P.; Ivanou, D.; Santos, F.; Azeyedo, J.; Mendes, A. Synthesis of host-guest hematite photoelectrodes for solar water splitting. *Chemnanomat* **2019**, 5, 911-920.
- (17) Yu, W.; Chen, J.; Shang, T.; Chen, L.; Gu, L.; Peng, T. Direct Z-scheme g-C<sub>3</sub>N<sub>4</sub>/WO<sub>3</sub> photocatalyst with atomically defined junction for H<sub>2</sub>-production. *Appl. Catal. B Environ.* **2017**, 219, 693-704.
- (18) Li, H.; Zhao, F.; Zhang, J.; Luo, L.; Xiao, X.; Huang, Y.; Ji, H.; Tong, Y. A g-C<sub>3</sub>N<sub>4</sub>/WO<sub>3</sub> photoanode with exceptional ability for photoelectrochemical water splitting. *Mate. Chem. Front.* **2017**, 1, 338-342.
- (19) Pinto, F.; Wilson, A.; Moss, B.; Kafizas, A. Systematic exploration of WO<sub>3</sub>/TiO<sub>2</sub> heterojunction phase space for applications in photoelectrochemical water splitting. *J. Phys. Chem. C* **2022**, 126, 871-884.
- (20) Wei, P.; Lin, K.; Meng, D.; Xie, T.; Na, Y. Photoelectrochemical performance for water oxidation improved by molecular nickel porphyrin-integrated WO<sub>3</sub>/TiO<sub>2</sub> photoanode. *Chemsuschem* **2018**, 11, 1746-1750.
- (21) Sun, W.; Wang, D.; Rahman, Z. U.; Wei, N.; Chen, S. 3D hierarchical WO<sub>3</sub> grown on TiO<sub>2</sub> nanotube arrays and their photoelectrochemical performance for water splitting. *J. Alloys Compd.* **2017**, 695, 2154-2159.
- (22) Khare, C.; Sliozberg, K.; Meyer, R.; Savan, A.; Schuhmann, W.; Ludwig, A. Layered WO<sub>3</sub>/TiO<sub>2</sub> nanostructures with enhanced photocurrent densities. *Int. J. Hydrogen Energy* **2013**, 38, 15954-15964.
- (23) Zhang, Y. F.; Zhu, Y. K.; Lv, C. X.; Lai, S. J.; Xu, W. J.; Sun, J.; Sun, Y. Y.; Yang, D. J. Enhanced visible-light photoelectrochemical performance via chemical vapor deposition of Fe<sub>2</sub>O<sub>3</sub> on a WO<sub>3</sub> film to form a heterojunction. *Rare Metals* **2020**, 39, 841-849.
- (24) Kim, E.; Kim, S.; Choi, Y. M.; Park, J. H.; Shin, H. Ultrathin hematite on mesoporous WO<sub>3</sub> from atomic layer deposition for minimal charge recombination. *ACS Sustain. Chem. Eng.* **2020**, 8, 11358-11367.
- (25) Memar, A.; Phan, C. M.; Tade, M. O. Photocatalytic activity of WO<sub>3</sub>/Fe<sub>2</sub>O<sub>3</sub> nanocomposite photoanode. *Int. J. Hydrogen Energy* **2015**, 40, 8642-8649.
- (26) Sadhasivam, S.; Gunasekaran, A.; Anbarasan, N.; Mukilan, N.; Jeganathan, K. CdS and CdSe nanoparticles activated 1D TiO<sub>2</sub> hetero-structure nanoarray photoelectrodes for enhanced photoelectrocatalytic water splitting. *Int. J. Hydrogen Energy* **2021**, 46, 26381-26390.
- (27) Qiu, Y.; Pan, Z.; Chen, H.; Ye, D.; Guo, L.; Fan, Z.; Yang, S. Current progress in developing metal oxide nanoarrays-based photoanodes for photoelectrochemical water splitting. *Sci. Bull.* **2019**, 64, 1348-1380.
- (28) Pu, Y.; Wang, G.; Chang, K.; Ling, Y.; Li, Y. Au nanostructure-decorated TiO<sub>2</sub> nanowires exhibiting photoactivity across entire UV-visible region for photoelectrochemical water splitting. *Nano Lett.* **2013**, 13, 3817-3823.
- (29) Luo, Z.; Wang, T.; Zhang, J.; Li, C.; Li, H.; Gong, J. Dendritic hematite nanoarray photoanode modified with a conformal titanium dioxide inter-layer for effective charge collection. *Angew. Chem. Int. Ed.* **2017**, 56, 12878-12882.
- (30) Peng, G.; Lu, H.; Liu, Y.; Fan, D. The construction of a single-crystalline SbSI nanorod array-WO<sub>3</sub> heterostructure photoanode for high PEC performance. *Chem. Commun.* **2021**, 57, 335-338.
- (31) Gimenes, D. T.; Nossol, E. Effect of light source and applied potential in the electrochemical synthesis of Prussian blue on carbon nanotubes. *Electrochim. Acta* **2017**, 251, 513-521.
- (32) Mao, G.; Li, C.; Li, Z.; Xu, M.; Wu, H.; Liu, Q. Efficient charge migration in TiO<sub>2</sub>@PB nanorod arrays with core-shell structure for photoelectrochemical water splitting. *CrystEngComm* **2022**, 24, 2567-2574.
- (33) Wu, H.; Liu, Q.; Zhang, L.; Tang, Y.; Wang, G.; Mao, G. Novel nanostructured WO<sub>3</sub>@Prussian blue heterojunction photoanodes for efficient photoelectrochemical water splitting. *ACS Appl. Energy Mater.* **2021**, 4, 12508-12514.
- (34) Cao, L.; Liu, Y.; Zhang, B.; Lu, L. In situ controllable growth of Prussian blue nanocubes on reduced graphene oxide: facile synthesis and their application as enhanced nanoelectrocatalyst for H<sub>2</sub>O<sub>2</sub> reduction. *ACS Appl. Mater. Inter.* **2010**, 2, 2339-2346.
- (35) Li, Y.; Hu, J.; Yang, K.; Cao, B.; Li, Z.; Yang, L.; Pan, F. Synthetic control of Prussian blue derived nano-materials for energy storage and conversion application. *Mater. Today Energy* **2019**, 14, 100332.
- (36) Hu, M.; Belik, A. A.; Imura, M.; Mibu, K.; Tsujimoto, Y.; Yamauchi, Y. Synthesis of superparamagnetic nanoporous iron oxide particles with hollow interiors by using Prussian blue coordination polymers. *Chem. Mater.* **2012**, 24, 2698-2707.
- (37) Zakaria, M. B.; Belik, A. A.; Liu, C. H.; Hsieh, H. Y.; Liao, Y. T.; Malgras, V.; Yamauchi, Y.; Wu, K. C. W. Prussian blue derived nano-porous iron oxides as anticancer drug carriers for magnetic-guided chemotherapy. *Chem. Asian J.* **2015**, 10, 1457-1462.
- (38) Wang, Y.; Wang, Y.; Zhao, J.; Chen, M.; Huang, X.; Xu, Y. Efficient production of H<sub>2</sub>O<sub>2</sub> on Au/WO<sub>3</sub> under visible light and the influencing factors. *Appl. Catal. B* **2021**, 284, 119691-119702.
- (39) Ma, M.; Zhang, K.; Li, P.; Jung, M. S.; Jeong, M. J.; Park, J. H. Dual oxygen and tungsten vacancies on a WO<sub>3</sub> photoanode for enhanced water oxidation. *Angew. Chem. Int. Ed.* **2016**, 128, 11998-12002.
- (40) Ma, J.; Mao, K.; Low, J.; Wang, Z.; Xi, D.; Zhang, W.; Ju, H.; Qi, Z.; Long, R.; Wu, X.; Song, L.; Xiong, Y. Efficient photoelectrochemical conversion of methane into ethylene glycol by WO<sub>3</sub> nanobar arrays. *Angew. Chem. Int. Ed.* **2021**, 133, 9443-9447.
- (41) Iandolo, B.; Wickman, B.; Zoric, I.; Hellman, A. The rise of hematite: origin and strategies to reduce the high onset potential for the oxygen evolution reaction. *J. Mater. Chem. A* **2015**, 3, 16896-16912.
- (42) Chai, H.; Gao, L.; Wang, P.; Li, F.; Hu, G.; Jin, J. In<sub>2</sub>S<sub>3</sub>/F-Fe<sub>2</sub>O<sub>3</sub> type-II heterojunction bonded by interfacial S-O for enhanced charge separation and transport in photoelectrochemical water oxidation. *Appl. Catal. B Environ.* **2022**, DOI 10.1016/j.apcatb.2021.121011.
- (43) Zhang, M.; Luo, W.; Li, Z.; Yu, T.; Zou, Z. Improved photoelectrochemical responses of Si and Ti codoped α-Fe<sub>2</sub>O<sub>3</sub> photoanode films. *Appl. Phys. Lett.* **2010**, 97, 042105-042105.
- (44) Mei, B. A.; Munteshari, O.; Lau, J.; Dunn, B.; Pilon, L. Physical interpretations of nyquist plots for EDLC electrodes and devices. *J. Phys. Chem. C* **2018**, 122, 194-206.
- (45) Sivula, K.; Formal F. L.; Gratzel, M. WO<sub>3</sub>-Fe<sub>2</sub>O<sub>3</sub> photoanodes for water splitting: a host scaffold, guest absorber approach. *Chem. Mater.* **2009**, 21, 2862-2867.
- (46) Wu, Q.; Bu, Q.; Li, S.; Lin, Y.; Zou, X.; Wang, D.; Xi, T. Enhanced interface charge transfer via n-n WO<sub>3</sub>/Ti-Fe<sub>2</sub>O<sub>3</sub> heterojunction formation for water splitting. *J. Alloys Compd.* **2019**, 803, 1105-1111.

Received: April 12, 2022

Accepted: May 14, 2022

Published online: May 31, 2022

Published: July 25, 2022